Surface & Coatings Technology 476 (2024) 130244

Contents lists available at ScienceDirect

Surface & Coatings Technology

journal homepage: www.elsevier.com/locate/surfcoat

Effect of Mo content on the microstructure and mechanical properties of $CoCrFeNiMo_x$ HEA coatings deposited by high power impulse magnetron sputtering

Valentina Zin [a], Francesco Montagner [a], Enrico Miorin [a], Cecilia Mortalò [a], Riccardo Tinazzi [b], Giovanni Bolelli [b], Luca Lusvarghi [b], Alessandro Togni [b,*], Stefano Frabboni [c], Giancarlo Gazzadi [d], Andrea Mescola [d], Guido Paolicelli [d], Lidia Armelao [e,f], Silvia Maria Deambrosis [a,*]

[a] National Research Council of Italy (CNR), Institute of Condensed Matter Chemistry and Technologies for Energy (ICMATE), Corso Stati Uniti, 4, 35127 Padova, Italy
[b] Department of Engineering "Enzo Ferrari", University of Modena and Reggio Emilia, Via P. Vivarelli 10, 41125 Modena, Italy
[c] Department of Physics, University of Modena and Reggio Emilia, Via G. Campi 213/A, 41125 Modena, Italy
[d] CNR-NANO, Istituto Nanoscienze, Consiglio Nazionale delle Ricerche, Via Campi 213/A, 41125 Modena, Italy
[e] Department of Chemical Sciences (DiSC), University of Padova, via F. Marzolo 1, 35131 Padova, Italy
[f] Department of Chemical Sciences and Materials Technologies (DSCTM), National Research Council (CNR), Piazzale A. Moro 7, 00185 Roma, Italy

ARTICLE INFO

Keywords:
High power impulse magnetron co-sputtering
High entropy alloys
$CoCrFeNiMo_x$
Microstructure
Mechanical properties

ABSTRACT

In this work, $CoCrFeNiMo_x$ high entropy alloy (HEA) films were deposited by High Power Impulse Magnetron Sputtering (HiPIMS) using pure Mo and equiatomic CoCrFeNi targets. The effect of Mo content on the microstructure, residual stress state, and mechanical properties of the films was investigated in the range of 0–20 at.%. All films exhibited a columnar growth morphology and a high density of planar defects. Increasing the Mo content promoted the formation of a fine-grained structure and induced the transformation from a single face-centered cubic (FCC) phase to a mixture of FCC and body-centered cubic (BCC) phases. All produced films displayed a compressive residual stress state regardless of the Mo concentration. In terms of mechanical properties, the hardness of the films increased with increasing Mo content due to solid solution and grain boundary strengthening, along with the formation of a hard BCC phase. On the other hand, the elastic modulus decreased, likely due to the formation of an amorphous phase at higher Mo concentrations.

1. Introduction

High entropy alloys (HEAs), first proposed by Yeh et al. [1] and Cantor et al. [2] in the early 2000s, have garnered significant interest owing to their groundbreaking compositional design. Unlike conventional alloys, HEAs consist of five or more principal elements, each with an atomic fraction ranging from 5 to 35 at.%. Due to the complexity of mixing numerous different elements, the high configurational entropy of HEAs is believed to promote the formation of simple solid solution phases with face-centered cubic (FCC), body-centered cubic (BCC), or hexagonal close-packed (HCP) structures rather than intermetallic compounds [3]. They have been mainly studied because of their good response in terms of mechanical properties [4,5], oxidation resistance [6,7], magnetic properties [8], radiation resistance [9], wear resistance [10], and catalytic activity [11] ascribable to a sort of cocktail effect [12,13]. One noteworthy example is the FCC-structured CoCrFeMnNi HEA, also known as the Cantor alloy, and its subsets like CoCrFeNi, which have been extensively investigated due to their remarkable ductility and fracture toughness [14]. However, these alloys exhibit relatively low hardness and yield strength at room temperature, which limits their potential applications [15,16]. To overcome these limitations and enhance the mechanical properties of HEAs, researchers have explored the addition of various elements, such as Al [17,18], Mo [19–22], Nb [23], Ti [24], and V [25,26]. These elements, having larger atomic radii, induce lattice distortion and promote the formation of a secondary phase separated from the FCC matrix [27]. Among these elements, the incorporation of Mo has proven promising for improving the strength of FCC-structured HEAs. This enhancement occurs not only

* Correspondig authors.
E-mail addresses: alessandro.togni@unimore.it (A. Togni), silviamaria.deambrosis@cnr.it (S.M. Deambrosis).

https://doi.org/10.1016/j.surfcoat.2023.130244
Received 27 October 2023; Received in revised form 21 November 2023; Accepted 22 November 2023
Available online 27 November 2023

through solid solution strengthening but also via the precipitation of hard intermetallic phases, as evidenced in the $CoCrFeNiMo_x$ [19–21] and $CoCrFeMnNiMo_x$ [22] systems.

The inclusion of five elements in the alloy system is more beneficial for the solid solution strengthening effect when compared to four elements. Mo-containing alloys have been studied, exhibiting a microstructure characterized by either BCC or BCC + α phases (unidentified Mo-rich phase) and high compressive strengths, attributed to the formation of a strong but ductile FCC matrix and a hard BCC secondary phase [28,29]. In bulk cast alloys, Mo often tends to form hard intermetallic phases when combined with Co, Cr, Fe, and Ni elements, revealing an attractive combination of physical and mechanical properties [22].

Despite the numerous advantages offered by HEAs, the high costs of raw materials and the challenges associated with their fabrication using arc melting and casting methods still limit their effective applications. Consequently, researchers have explored HEAs in the form of thin films and coatings, thereby further expanding their application potential [30].

Various deposition methods, including magnetron sputtering [31,32], laser cladding [33], and electrodeposition [34], have been used to fabricate HEA films. Among these techniques, magnetron sputtering has emerged as a popular method for the deposition of HEA thin films, offering precise control over their composition, microstructure, and overall quality. High power Impulse Magnetron Sputtering (HiPIMS) represents one of the latest advancements of the magnetron sputtering technique [35]. Within this process, power is applied to the target in the form of short, unipolar pulses with low-duty cycles—typically <10 %—and frequencies below 10 kHz. This approach yields peak target power densities of the order of several kW/cm^2, thus generating plasmas characterized by electron densities of up to 10^{19} m^{-3}, accompanied by a significant fraction of ionized species. The resulting intensive ion bombardment enhances adatom mobility during film growth, ultimately leading to the formation of dense and smooth films [36,37]. Nonetheless, despite the advantages of HiPIMS and its potential for producing high-quality films with enhanced properties, only a limited number of studies have reported on the deposition of CoCrFeNi-based HEA films using this technique [38,39].

In light of these considerations, the current study addresses the deposition of $CoCrFeNiMo_x$ HEA films via HiPIMS, with the primary objective of investigating the relationship between the Mo content and the microstructure, residual stress state, and mechanical properties of the resulting films.

2. Methods

2.1. Film deposition

$CoCrFeNiMo_x$ HEA films with a thickness of ~3 μm were synthesized by HiPIMS using a lab-scale deposition system equipped with two HiPSTER 6 power supply units (Ionautics AB, Linköping, Sweden), each operating at an average power of up to 6 kW, and a HiPSTER 1 power supply unit (Ionautics AB, Linköping, Sweden) for substrate biasing, with a maximum average power of 1 kW. A HiPSTER Sync Unit (Ionautics AB, Linköping, Sweden) was used to synchronize the two HiPSTER 6 units and the HiPSTER 1 unit during the deposition process. Fig. 1 provides a schematic representation of the experimental setup. The films were deposited on 600 μm thick Si (100) substrates using two vacuum arc-melted targets: one made of CoCrFeNi and the other made of Mo, each having a diameter of 10 cm and a thickness of 0.3 cm. Before being placed into the deposition chamber, the substrates were cleaned in an ultrasonic bath with acetone and isopropanol, followed by drying with pure N_2. The targets were tilted at 45° relative to the substrate surface normal. The distance between the CoCrFeNi target and the substrates was kept constant at 120 mm, while the distance between the Mo target and the substrates was varied between 105 mm and 220 mm to tune the Mo content in the films. This is a way to perturb the deposition conditions as little as possible. Indeed, by increasing the target-substrate distance, despite a lower energy flux carried to the substrate (i.e., enhanced thermalization effect), all other deposition parameters remain virtually unchanged, including voltage, average current, and peak current. In addition, preliminary tests confirm that Mo content is a function of the ratio of the distances squared (i.e., $\text{at.\%}Mo_{D1} \sim at.\%$

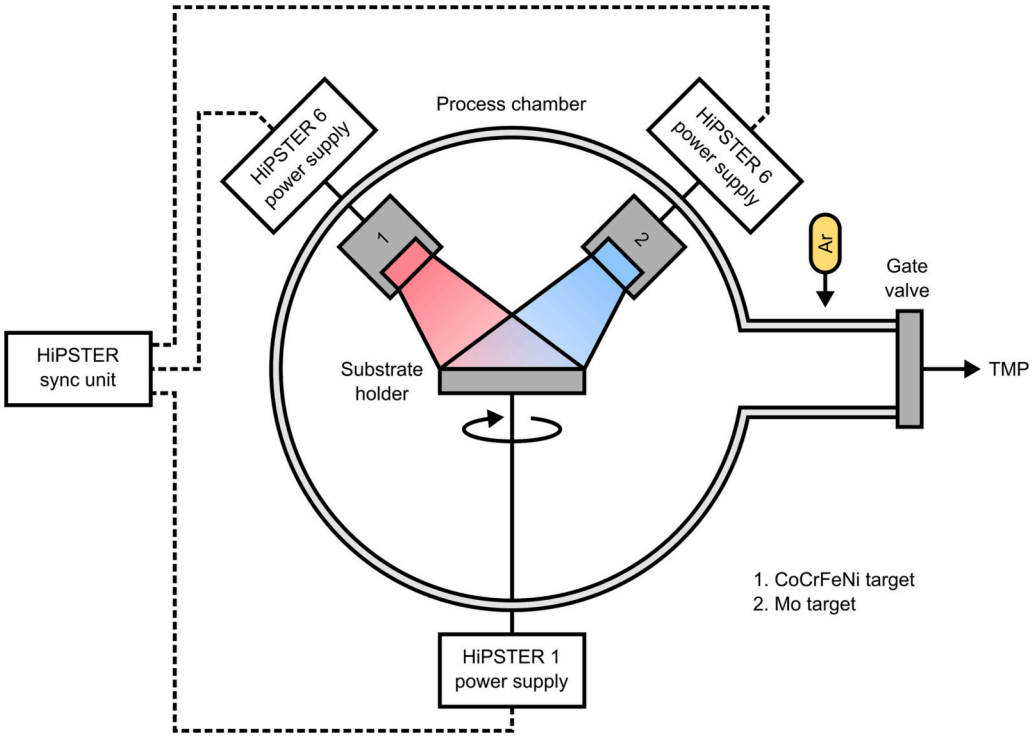

Fig. 1. Schematic representation of the deposition system.

$Mo_{D2} \times D2^2/D1^2$). Therefore, it is possible to predict the final composition of the coating with a good approximation.

Before deposition, the process chamber was evacuated to a base pressure of 10^{-5} Pa. During film growth, a total pressure of 0.5 Pa was maintained by flowing pure Ar into the chamber. The CoCrFeNi target was operated at an average power of 500 W, a frequency of 250 Hz, and a pulse width of 100 μs. On the other hand, the Mo target was operated at an average power of 100 W, a frequency of 250 Hz, and a pulse width of 75 μs. The substrate bias voltage was set at −105 V, with a frequency of 250 Hz and a pulse width of 200 μs. The substrate holder was rotated at 10 rpm to achieve a uniform film composition, later confirmed by energy-dispersive X-ray spectroscopy (EDS). Although no external heating was applied during deposition, the thermocouples near the substrate holder recorded an approximate temperature of 55 °C.

The discharge voltage and current were continuously monitored using a PicoScope 2406B oscilloscope (Pico Technology, St Neots, UK), and the recorded waveforms are illustrated in Fig. 2. Both CoCrFeNi and Mo targets displayed rectangular-shaped voltage peaks, reaching plateaus at 600 V and 500 V, respectively. The discharge current initially increased to 45 A for the CoCrFeNi target and 15 A for the Mo target, followed by a moderate decrease. The authors decided to use a synchronized bias voltage with an approximately zero delay time and a pulse width double compared to the cathode one (200 μs). With this operating mode, most of the ions produced during the source pulse is accelerated and should contribute to grow relatively hard coatings, while maintaining a rather low residual stress. In future work, the effect of varying the bias delay time and pulse length will also be investigated. Indeed, as reported for example in [40–42], ion mass spectrometry could be used to identify the target ion-rich portion of HiPIMS pulse and apply a synchronized substrate polarization with a proper delay time and pulse width to select the ion fraction, improve mechanical properties and reduce residual stress.

2.2. Film characterization

The surface morphology and chemical composition of the as-deposited films were analyzed using a Zeiss Sigma field-emission scanning electron microscope (FE-SEM, Carl Zeiss, Oberkochen, Germany) equipped with an Oxford X-Max energy-dispersive X-ray spectrometer (EDS, Oxford Instruments, Oxford, UK) operated at 15 kV.

Atomic force microscopy (AFM) measurements were conducted in tapping mode using an NT-MDT NTEGRA Aura microscope. Si cantilevers with a nominal tip radius of <10 nm, a force constant ranging from 0.3 to 0.8 N/m, and a resonance frequency between 20 and 40 KHz were used. Subsequently, the AFM data were processed using the Gwyddion software to determine the surface roughness parameters of the films.

The crystal structure of the films was investigated by X-ray diffraction (XRD) using an Empyrean X-ray diffractometer (Malvern Panalytical, Malvern, UK) equipped with a Cu-Kα radiation source operating at 40 kV and 40 mA. The XRD measurements were carried out in Bragg-Brentano geometry. The XRD patterns were recorded over a 2θ range of 30–110° with a resolution of 0.03° per step and a step time of 30 s. The obtained diffraction patterns were analyzed using the Match! ver. 3.8 software to identify the crystalline phases based on the positions of the detected peaks.

Transmission electron microscopy (TEM) and selected area electron diffraction (SAED) analyses were carried out using a TALOS F200S G2 S/TEM (Thermo Fisher Scientific, Waltham, MA, USA) equipped with a Schottky field emitter operated at 200 keV and two silicon drift detectors (SDDs) for energy-dispersive X-ray spectroscopy. Electron-transparent TEM samples were prepared by focused ion beam (FIB) milling after depositing a thin Pt layer on the surface to prevent damage, redeposition artifacts, and Ga implantation during the milling process. The FIB milling was carried out using an FEI Strata DB235M Dual Beam system (Thermo Fisher Scientific, Waltham, MA, USA) at an acceleration voltage of 30 kV, followed by final polishing at 5 kV to minimize any potential sample damage caused by Ga ions.

The residual stress state within the films was evaluated using the wafer curvature method based on Stoney's equation [43,44]. Magnetron-sputtered films commonly exhibit residual stresses, which cause bending deformation in the film-substrate system. Consequently, the residual stress state in the film can be estimated from the curvature of the deformed sample. The bending of the film-substrate system can be either concave or convex, depending on the nature of the stresses. Convex curvature is typically associated with compressive stresses and is conventionally represented by a negative sign, while concave curvature indicates tensile stresses and is conventionally denoted by a positive sign. The curvature of the films was measured using a DektakXT stylus profilometer (Bruker, Billerica, MA, USA). For each sample, a total of six traces were acquired, three for each main direction.

Nanoindentation measurements were performed using a NanoTest system (Micro Materials, Wrexham, UK) equipped with a diamond Berkovich tip (E = 1140 GPa and $\nu = 0.07$). The tests were conducted in depth-controlled mode, ensuring that the maximum penetration was less than one-tenth (1/10) of the film thickness to minimize any potential substrate influence on the measured mechanical properties [45]. For each sample, a set of 25 indentations was performed. The hardness and the elastic modulus of the films were then determined from the resulting load-displacement curves using the Oliver-Pharr method [46,47].

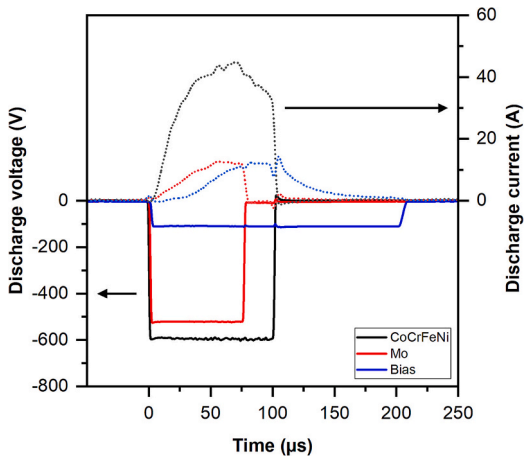

Fig. 2. Temporal evolution of the discharge voltage and current waveforms recorded during the HiPIMS process.

3. Results and discussion

3.1. Chemical composition and surface morphology

As described in Section 2.1, the Mo concentration in the films was controlled by adjusting the distance between the Mo target and the Si substrates, ranging from 105 to 220 mm. All remaining process parameters were maintained constant throughout the experimental campaign. The chemical composition of the as-deposited films analyzed by EDS is listed in Table 1. The Mo content shows an inversely proportional relationship to the Mo target-to-substrate distance, increasing from 5.2 to 19.8 at.% when the latter decreases from 220 to 105 mm. For convenience, the films with Mo concentrations of 0, 5.2, 9.2, 16.8, and 19.8 at.% are referred to as Mo0, Mo5, Mo10, Mo15, and Mo20, respectively. Clearly, an increase in Mo concentration results in a gradual decrease in the concentrations of the other elements. It is worth noting that, in all cases, the content of Co and Cr is slightly higher than that of Fe and Ni. This observation aligns with the findings of Wang et al. [48], who reported a similar behavior during the deposition of CoCrFeNi films using pulsed DC magnetron sputtering. Several factors, including the target composition and the different sputter yields of each element

Table 1
Chemical composition of the $CoCrFeNiMo_x$ HEA films as a function of the Mo target-to-substrate distance.

Sample	$D_{Mo\ target\text{-}to\text{-}substrate}$ (mm)	Chemical composition (at.%)				
		Fe	Cr	Ni	Co	Mo
Mo0	–	24.2 ± 0.3	27.2 ± 0.3	22.6 ± 0.4	26.0 ± 0.4	–
Mo5	220	22.7 ± 0.2	25.4 ± 0.1	21.8 ± 0.1	24.9 ± 0.1	5.2 ± 0.1
Mo10	160	21.5 ± 0.2	24.9 ± 0.2	20.4 ± 0.2	24.0 ± 0.2	9.2 ± 0.1
Mo15	120	19.4 ± 0.2	23.0 ± 0.1	18.1 ± 0.3	22.7 ± 0.2	16.8 ± 0.1
Mo20	105	18.5 ± 0.2	22.4 ± 0.1	17.1 ± 0.1	22.2 ± 0.2	19.8 ± 0.1

[49], may contribute to the observed variations in composition.

The top surface SEM micrographs of the films are presented in Fig. 3. The surfaces of the films containing low Mo concentrations, i.e., Mo0, Mo5, and Mo10, exhibit a granular morphology. On the other hand, the films with higher Mo content appear almost featureless.

The surface grain refinement was further evaluated via AFM. The AFM images are shown in Fig. 4, revealing a rounded grain-type surface morphology for the films containing lower Mo concentrations, Mo0, Mo5, and Mo10. In contrast, fine granular surfaces with small and densely packed grains are observed in the Mo-rich films, Mo15 and Mo20. The AFM data were used to determine the surface roughness of the films. The average surface roughness (Sa) and root mean square roughness (Sq) values are reported in Table 2. Sa decreases from 2.9 to 1.5 nm as the Mo content increases from 9.2 to 16.8 at.%. Similarly, Sq decreases from 3.5 to 1.9 nm with increasing Mo content above 9.2 at.%. These findings confirm that higher Mo contents lead to denser and smoother surfaces, which could significantly affect the mechanical

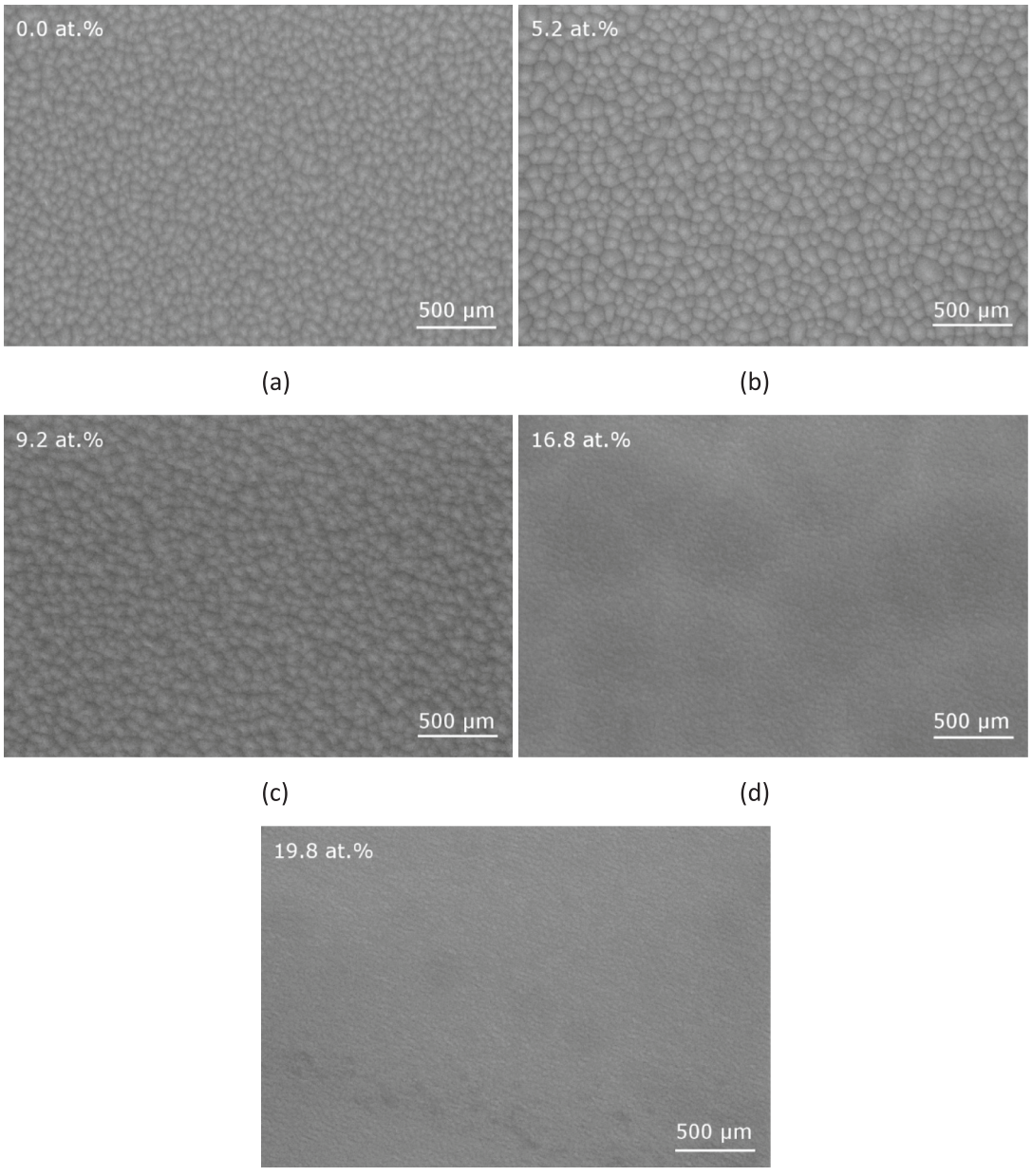

Fig. 3. SEM micrographs showing the top view of the (a) Mo0, (b) Mo5, (c) Mo10, (d) Mo15, and (e) Mo20 films.

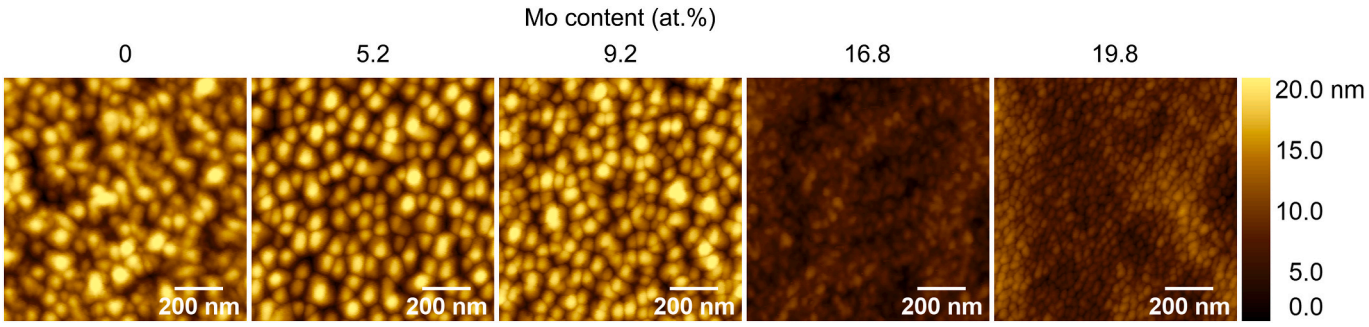

Fig. 4. AFM images of the surface of the $CoCrFeNiMo_x$ HEA films.

Table 2
Surface roughness parameters of the $CoCrFeNiMo_x$ HEA films obtained from the AFM measurements.

Sample	Mo content (at.%)	Sa (nm)	Sq (nm)	Sz (nm)
Mo0	–	3.0 ± 0.1	3.7 ± 0.1	24.4 ± 1.1
Mo5	5.2 ± 0.1	3.3 ± 0.1	4.1 ± 0.1	25.1 ± 1.5
Mo10	9.2 ± 0.1	2.9 ± 0.1	3.5 ± 0.1	22.4 ± 1.7
Mo15	16.8 ± 0.1	1.5 ± 0.1	1.9 ± 0.1	14.1 ± 2.3
Mo20	19.8 ± 0.1	1.7 ± 0.1	2.0 ± 0.1	15.0 ± 1.1

properties of the films.

3.2. Microstructure

XRD analysis was performed to investigate the crystal structure of the samples. Generally, when several alloying elements are combined in different proportions, the resulting structures may manifest as either face-centered cubic (FCC), body-centered cubic (BCC), or a combination of both [50,51]. However, it should be noted that in processes such as sputtering and thermal evaporation, the non-equilibrium conditions experienced during film growth could induce the formation of metastable alloy structures.

Fig. 5(a) shows the collected XRD patterns of the films as a function of the Mo content. The Mo-free film exhibits a crystalline structure consistent with an A1-type face-centered cubic (FCC) solid solution phase, evidenced by the diffraction peaks corresponding to the (111) and (222) planes of the FCC phase. This finding aligns with other sputtered CoCrFeNi films reported in the literature [83]. As the Mo content increases, the diffraction peaks of the FCC phase shift toward lower 2θ values, which could be attributed to the lattice distortion caused by the substitution of Co, Cr, Fe, and Ni with the larger Mo atoms [19,84]. Moreover, when the Mo content exceeds 9.2 at.%, two additional diffraction peaks appear at 2θ values of 41.1° and 90°, which are consistent with the (110) and (220) planes of a Mo-rich body-centered cubic (BCC) structure. This result is in line with the findings of Zhao et al. [52], who observed a transition in the phase structure of $FeCoNiCrMnMo_x$ films from a single FCC phase to a mixture of FCC and BCC phases upon Mo addition. Similarly, the coexistence of FCC and BCC phases has also been reported by Boakye et al. [53] in $CoCrFeNiMo_x$ HEA coatings. Unlike other elements in the alloy, Mo does not possess a stable FCC allotrope and does not form a single-phase FCC solid solution with any other element in the alloy [54]. Therefore, when the solubility of Mo in the matrix reaches its limit, the phase structure changes from a single-phase FCC structure to a dual-phase FCC + BCC structure. Furthermore, the FCC-related diffraction peaks gradually weaken and broaden with increasing Mo content, suggesting a decrease in crystallinity within the films. Specifically, the full width at half-maximum height (FWHM) of each peak progressively increases, indicating that the crystallite size reduces with increasing Mo concentration. The crystallite size distribution is known to have a significant impact on film properties such as mechanical strength, hardness, and surface finishing, and the formation of nanocrystalline grains is highly desirable for improving the mechanical properties of HEA films [55,56]. Here, the crystallite size of the FCC phase was estimated in accordance with the Scherrer formula [57]. The results are illustrated in Fig. 5 (b) and reveal a progressive decrease in average crystallite size with growing Mo content. In the dual-phase region, the interphase boundaries lead to reduced grain growth rates and smaller-sized grains, acting as obstacles for grain boundary migration [58]. In addition, the XRD patterns of the Mo5, Mo10, and Mo15 films exhibit a further unidentified peak at 38.7°,

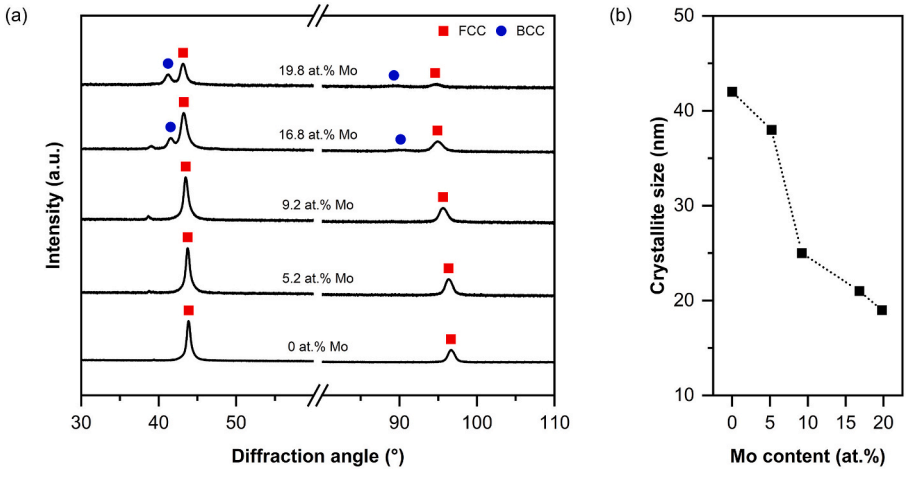

Fig. 5. (a) XRD patterns and (b) crystallite size of $CoCrFeNiMo_x$ HEA films as a function of Mo content.

which could be attributed to an intermetallic phase, as already observed in bulk $CoCrFeNiMo_x$ HEAs [19–21,59]. However, the reason behind the absence of this phase in the Mo20 film, contradicting previous findings in the literature, remains unclear and requires further investigation.

To further investigate the evolution of the microstructure with varying Mo content, the Mo5 and Mo20 films were selected for TEM observation. Fig. 6 (a-b) shows their cross-sectional bright-field TEM images, together with their corresponding SAED patterns (Fig. 6 (c-d)). Both films exhibit a microstructure consisting of nanometer-sized columnar grains oriented nearly perpendicular to the substrate surface. The average columnar grain width decreases from approximately a hundred nanometers in the Mo5 film to just a few tens of nanometers in the Mo20 film, which is in line with SEM and AFM results. Furthermore, a significant number of stacking faults and nanotwins are observed within the columnar grains. The formation of such planar defects is attributed to the low stacking fault energy (20–25 $mJ{\cdot}m^{-2}$) of these alloys [60]. Additionally, the atomic peening effect [61] induced during magnetron sputtering processes has been proposed as a contributing factor to the generation of nanotwinned structures in sputtered CoCrFeNi-based HEA films [62,63]. The SAED patterns of both samples show distinct (111) and (222) reflections of the FCC structure (FCC (111) → d = 0.206 nm; FCC (222) → d = 0.103 nm). However, in the Mo20 film, additional diffraction rings corresponding to the (110), (211), and (220) planes of the BCC phase are observed (BCC (110) → d = 0.222 nm; BCC (211) → d = 0.128 nm; BCC (220) → d = 0.110 nm), indicating the coexistence of a minor amount of BCC phase with the dominant FCC phase, which aligns with the XRD results shown in Fig. 5 (a). Moreover, the SAED pattern of the same film reveals a slightly diffuse ring, suggesting the presence of a poorly crystallized structure or an amorphous structure embedded within the FCC matrix. A similar behavior has also been reported in sputtered $(CoCrFeMnNi)_{100-x}Mo_x$ HEA films, where an excessive addition of Mo promoted the formation of an amorphous phase [64], thus affecting the mechanical properties of the produced films. In fact, as nanotwins obstacle the dislocation motion, the HEA films are expected to exhibit superior hardness compared to their bulk counterparts. At the same time, the presence of the amorphous phase could decrease their elastic modulus. This is because the elastic reaction force, when trying to move atoms from their actual positions, is less than it would be if they were in their equilibrium sites [65].

The requirements for the formation of a single solid-solution phase in HEAs can generally be regarded as an extension of the Hume-Rothery rules [66]. In HEAs, unlike conventional alloys, all elements can be considered as solute atoms, each having an equal probability of occupying lattice sites to form a solid solution [67]. Previous studies [50,68,69] have demonstrated that the prediction of single solid solutions in HEAs, along with their microstructure, relies on various thermodynamic parameters, such as the atomic size difference (δ), the ratio of entropy to enthalpy (Ω), the Pauling electronegativity difference ($\Delta\chi$), and the valence electron concentration (VEC). These parameters are

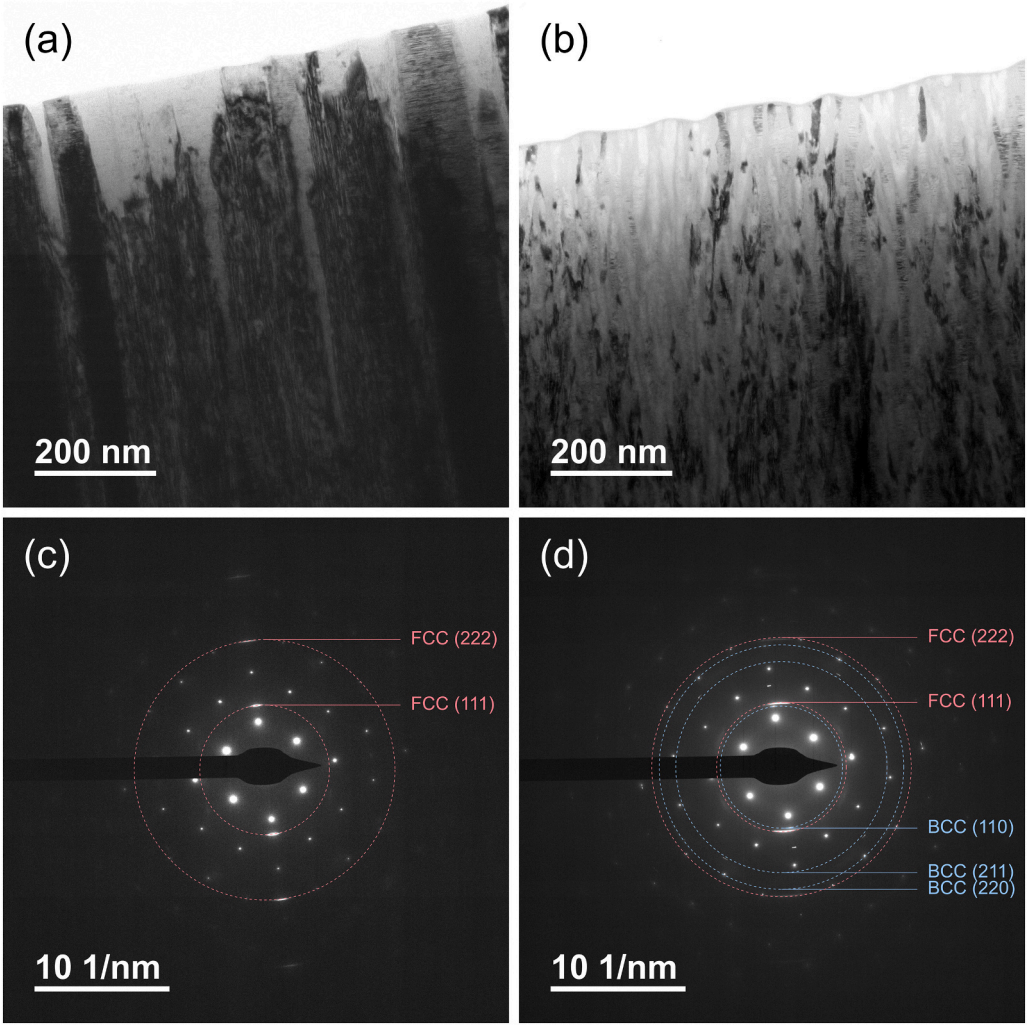

Fig. 6. Cross-sectional bright-field TEM images and the corresponding SAED patterns of the (a, c) Mo5 and (b, d) Mo20 films. Note that the bright spots in the SAED patterns are single-crystal reflections arising from the Si substrate, serving as references for interplanar distance calibration.

defined as follows [50,68,70]:

$$\delta = \sqrt{\sum_{i=1}^{n} c_i \left(1 - \frac{r_i}{\bar{r}}\right)^2} \quad (1)$$

$$\Omega = \frac{T_m \Delta S_{mix}}{|\Delta H_{mix}|} \quad (2)$$

$$\Delta\chi = \sqrt{\sum_{i=1}^{n} c_i (\chi_i - \bar{\chi})^2} \quad (3)$$

$$VEC = \sum_{i=1}^{n} c_i (VEC)_i \quad (4)$$

where n is the total number of elements, c_i and c_j are the atomic fractions of the ith or jth elements, respectively, r_i is the atomic radius of the ith element, $\bar{r}$ is the average atomic radius, T_m is the melting point, ΔS_{mix} is the entropy of mixing, ΔH_{mix} is the enthalpy of mixing, χ_i is the Pauling electronegativity of the ith element, and $(VEC)_i$ is the valence electron concentration of the ith element.

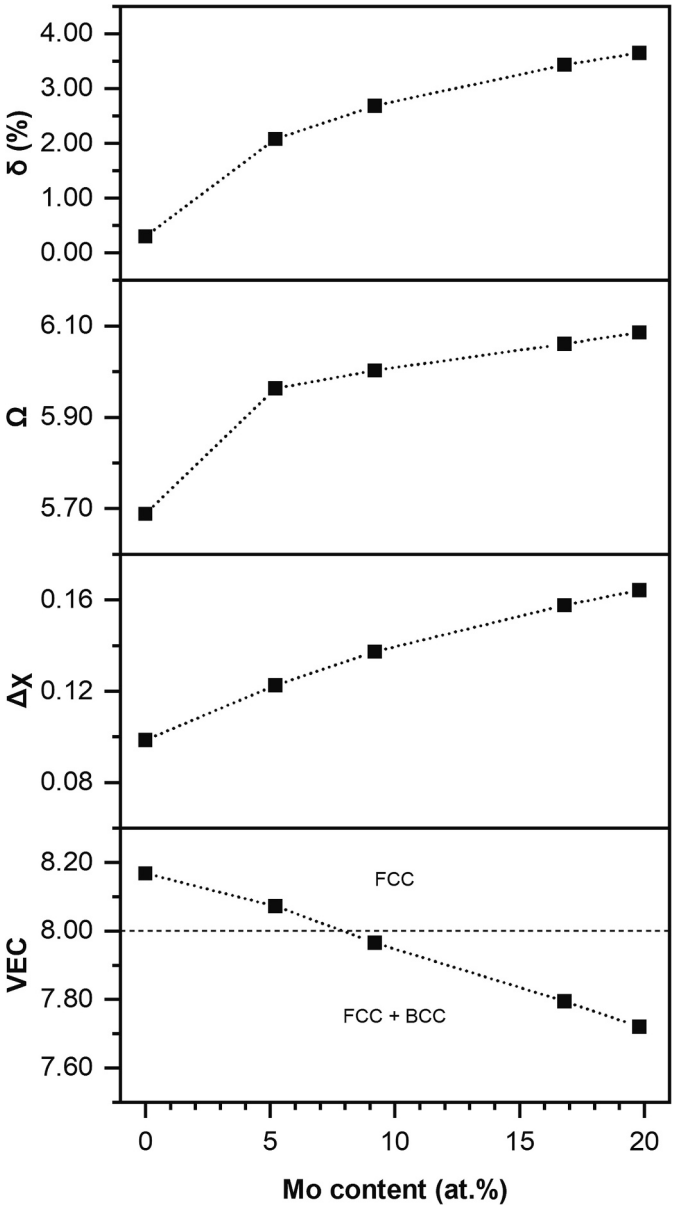

Fig. 7. Trends of the δ, Ω, Δχ, and VEC parameters as a function of Mo content in the fabricated CoCrFeNiMo$_x$ HEA films.

The calculated results for the CoCrFeNiMo$_x$ HEA films are presented in Fig. 7 as a function of the Mo content. The data required for these calculations were taken from [71,72]. According to Yang and Zhang [68], the solid solution phase in HEAs is likely to form when $\Omega \geq 1.1$ and $\delta \leq 6.6$ %. Generally, a large value of δ either promotes the formation of amorphous phases or ordered intermetallic compounds. Conversely, when the atomic size difference between components is relatively small, the different atoms can easily substitute for each other, occupying the lattice sites to form a solid solution. All the films analyzed in this study exhibit Ω and δ values falling within the established limits for the formation of a solid solution, as reported in [68]. It is noteworthy, however, that the Mo15 and Mo20 films displayed the highest δ values, suggesting the potential formation of an amorphous microstructure, as observed in the SAED patterns.

Later, Yang et al. [69] discovered that the electronegativity difference, Δχ, also plays a significant role in stabilizing solid solution phases in HEAs. Larger Δχ values promote the formation of compounds rather than solid solutions, as highly electronegative elements tend to acquire electrons from electropositive atoms. According to their findings, values of $\Delta\chi \leq 0.175$ promote the formation of solid solutions rather than intermetallic phases [69]. In the case of Mo15 and Mo20 samples, Δχ is close to the threshold value of 0.175, which might suggest the possible formation of minor amounts of ordered phases, as observed in the XRD patterns.

In another study, Guo et al. [50] proposed the use of the valence electron concentration (VEC) to predict the stability of BCC and FCC solid solution phases in HEAs primarily containing *3d* and/or *4d* transitional metals. The FCC phase is likely to form when VEC is ≥8, while a sole BCC phase is expected when VEC < 6.87. If VEC falls between 6.87 and 8 both FCC and BCC phases coexist. Occasionally, the BCC phase may also appear as a minor phase at the boundary value if VEC = 8.0. In the present study, the VEC values are higher than 8 up to a Mo content of approximately 10 at.%, indicating a tendency toward the formation of an FCC phase. On the other hand, for the Mo15 and Mo20 samples, the VEC values are 7.58 and 7.40, respectively, meeting the criteria for the formation of a dual-phase structure [50]. In the case of the Mo10 film, although the VEC is <8, thereby suggesting the formation of an FCC + BCC structure, only an FCC phase was detected by XRD.

3.3. Residual stress state and mechanical properties

The residual stress state within the films was estimated using the wafer curvature method. Several profiles were collected along both the Si (100) reference substrate and the coated samples to discern alterations in curvature after film deposition. The obtained results are presented in Table 3.

Except for the Mo-free sample, which shows negligible curvature and hence no measurable residual stress (i.e., close to 0 GPa), all the films exhibit a compressive residual stress state. The highest stress value of 1 GPa is observed in the Mo10 film. As the Mo content exceeds 9.2 at.%, the absolute magnitude of the residual stress progressively decreases to approximately 530 MPa. This reduction in stress levels coincides with the appearance of the BCC phase alongside the FCC phase. As previously discussed, Mo possesses a relatively larger atomic size compared to the other elements. Similar to the effect observed when adding Al to

Table 3
Estimated residual stresses and mechanical properties of CoCrFeNiMo$_x$ HEA films as a function of the Mo content.

Sample	Mo content (at.%)	σ (GPa)	H (GPa)	E (GPa)
Mo0	–	n. a.	9.62 ± 0.32	264.85 ± 9.91
Mo5	5.2 ± 0.1	−0.72 ± 0.13	9.68 ± 0.38	259.27 ± 7.92
Mo10	9.2 ± 0.1	−1.00 ± 0.18	9.99 ± 0.46	270.15 ± 15.36
Mo15	16.8 ± 0.1	−0.88 ± 0.03	11.13 ± 0.76	243.10 ± 12.33
Mo20	19.8 ± 0.1	−0.53 ± 0.06	11.49 ± 0.36	233.34 ± 5.24

$Al_xCoCrFeNi$ HEAs [73], an increase in Mo content is expected to lead to the accumulation of atomic-level strains, destabilizing the FCC structure and triggering the FCC-to-BCC transition. The lower packing efficiency of the BCC structure compared to the FCC structure could result in a partial release of strain energy, leading to the observed reduction in residual stress levels.

The values of hardness and elastic modulus of the films are shown in Table 3 as a function of the Mo content. Compared to bulk Mo-containing HEA alloys, the films produced in this work demonstrate a similar trend of increasing hardness with increasing Mo content [20,84], ranging from 9.6 GPa for the Mo0 film to 11.5 GPa for the Mo20 film, exhibiting significantly higher hardness values. It can be attributed to the fine-grained structure and the large fraction of planar defects found in the films [74,75], while the observed increase in hardness with increasing Mo content is likely related to the combined effect of solid solution strengthening, formation of the BCC phase, grain refinement, and the presence of a nanotwinned structure [52]. Firstly, the atomic size difference between Mo and the other constituents results in local lattice distortion due to Mo incorporation, as evidenced by the detected peak shifting in the XRD patterns (Fig. 5 (a)). As Mo atoms occupy lattice sites within the crystal structure, the associated lattice distortion contributes to a more pronounced solid solution strengthening effect, ultimately leading to enhanced film hardness [76]. Secondly, when the Mo content exceeds 9.2 at.%, a BCC phase forms in addition to the existing FCC phase, resulting in increased film hardness, as BCC-structured HEAs typically exhibit higher strength and lower plasticity compared to FCC-structured HEAs [3]. In addition, the increased density of phase boundaries resulting from the phase transformation creates additional obstacles for dislocation movement, further strengthening the film [22]. Similarly, grain boundary strengthening also contributes to the observed higher hardness values at higher Mo contents. The SEM and AFM analyses reveal a decrease in the crystallite size of the films as the Mo content increases. According to the Hall-Petch relationship [77,78], the hardness of the films increases accordingly.

In addition to grain and phase boundary strengthening, stacking faults and nanotwins can also provide additional obstacles to dislocation motion, resulting in a further strengthening effect [79–82]. Nevertheless, since the fraction of twinned grains is similar in both Mo5 and Mo20 films, as demonstrated in Fig. 6 (a-b), solid solution strengthening, grain-size strengthening, and the formation of harder ordered phases could be considered as the main factors responsible for the increase in hardness with the Mo content. In contrast, an evident contribution of residual stress is not accounted for, since the trend of compressive stress values does not follow the observed hardness variation.

The elastic modulus tends to decrease as the BCC phase appears in the microstructure of the deposited films, reaching a minimum value of 233 ± 5 GPa in the Mo20 film. The observed reduction could be attributed to the simultaneous formation of an amorphous phase at higher Mo concentrations, as evidenced by the slightly diffuse ring in the SAED pattern. Similar findings have also been reported by Fang et al. [62], who observed a decrease in the elastic modulus in $CoCrFeMnNiV_x$ films upon increasing V content due to the formation of an amorphous structure. In fact, amorphous structures are known to exhibit lower elastic moduli compared to their crystalline counterparts. Consequently, the observed decrease in the elastic modulus beyond a Mo content of 9.2 at.% can plausibly be attributed to the formation of the amorphous structure.

4. Conclusions

In this work, $CoCrFeNiMo_x$ (x = 0, 5, 10, 15, and 20 at.%) HEA films were deposited by HiPIMS to investigate the effect of Mo content on the morphology, microstructure, residual stress state, and mechanical properties of the resulting films.

The microstructure of the produced films consisted of columnar grains with a high density of stacking faults and nanotwins. With increasing Mo content, the crystalline structure changed from a single face-centered cubic (FCC) phase to a duplex FCC + body-centered cubic (BCC) structure, resulting in a reduced grain size due to the higher density of interphase boundaries. Further addition of Mo led to the formation of a highly disordered/amorphous phase.

Residual stress measurements indicated an initial increase in compressive stress values with increasing Mo content, possibly due to solid solution strengthening. However, as the Mo content continued to rise, the stress levels decreased, likely attributed to the formation of the BCC phase.

In terms of mechanical properties, the hardness of the films increased with increasing Mo content. A maximum hardness value exceeding 11 GPa was found for the Mo20 film, which was mainly attributed to the solid solution strengthening, formation of hard BCC phase, and grain refinement. This hardness is much higher than that of the bulk materials with comparable composition, primarily due to the fine columnar grain size, the abundance of planar defects, and the compressive residual stress state within the films. On the other hand, the elastic modulus decreased for Mo contents above 9.2 at.%, probably due to the formation of the amorphous phase.

Aknowledgements

This research work was partially financed as part of a research programme for the electricity system (RdS 2019-2021), thanks to an agreement between the Italian Ministry of Economic Development and the National Research Council of Italy.

CRediT authorship contribution statement

Valentina Zin: Formal analysis, Investigation, Methodology, Validation, Visualization, Writing – original draft, Writing – review & editing. **Francesco Montagner:** Conceptualization, Investigation, Methodology, Writing – original draft. **Enrico Miorin:** Conceptualization, Formal analysis, Writing – review & editing. **Cecilia Mortalò:** Formal analysis, Writing – review & editing. **Riccardo Tinazzi:** Formal analysis, Investigation. **Giovanni Bolelli:** Validation, Writing – review & editing. **Luca Lusvarghi:** Supervision, Writing – review & editing. **Alessandro Togni:** Formal analysis, Investigation, Validation, Visualization, Writing – review & editing. **Stefano Frabboni:** Investigation, Writing – review & editing. **Giancarlo Gazzadi:** Investigation. **Andrea Mescola:** Investigation. **Guido Paolicelli:** Investigation. **Lidia Armelao:** Funding acquisition. **Silvia Maria Deambrosis:** Conceptualization, Methodology, Project administration, Supervision, Validation, Writing – review & editing.

Declaration of competing interest

The authors declare that they have no known competing financial interests or personal relationships that could have appeared to influence the work reported in this paper.

Data availability

Data will be made available on request.

References

[1] J.W. Yeh, et al., Nanostructured high-entropy alloys with multiple principal elements: novel alloy design concepts and outcomes, Adv. Eng. Mater. 6 (5) (2004) 299–303, https://doi.org/10.1002/adem.200300567.
[2] B. Cantor, I.T.H. Chang, P. Knight, A.J.B. Vincent, Microstructural development in equiatomic multicomponent alloys, Mater. Sci. Eng. A 375–377 (1–2) (2004) 213–218, https://doi.org/10.1016/j.msea.2003.10.257. SPEC. ISS.
[3] Y. Zhang, et al., Microstructures and properties of high-entropy alloys, in: Progress in Materials Science vol. 61, Elsevier Ltd, 2014, pp. 1–93, https://doi.org/10.1016/j.pmatsci.2013.10.001.

[4] E.P. George, et al., High entropy alloys: a focused review of mechanical properties and deformation mechanisms, Acta Mater. 188 (2020) 435–474, https://doi.org/10.1016/j.actamat.2019.12.015.

[5] Y.K. Kim, et al., Superior temperature-dependent mechanical properties and deformation behavior of Equiatomic CoCrFeMnNi high-entropy alloy additively manufactured by selective laser melting, Sci. Rep. 10 (1) (2020) 1–13, https://doi.org/10.1038/s41598-020-65073-2.

[6] Y.Q. Jiang, et al., Evolution in microstructure and corrosion behavior of AlCoCrxFeNi high-entropy alloy coatings fabricated by laser cladding, J. Alloys Compd. 775 (2019) 1–14, https://doi.org/10.1016/j.jallcom.2018.10.091.

[7] X.W. Qiu, et al., Corrosion performance of Al2CrFeCoxCuNiTi high-entropy alloy coatings in acid liquids, J. Alloys Compd. 708 (2017) 353–357, https://doi.org/10.1016/j.jallcom.2017.03.054.

[8] F. Chang, et al., Thermal stability and oxidation resistance of FeCrxCoNiB high-entropy alloys coatings by laser cladding, Surf. Coating. Technol. 359 (2019) 132–140, https://doi.org/10.1016/j.surfcoat.2018.12.072.

[9] T.F. Yang, et al., Structural damage and phase stability of Al0.3CoCrFeNi high entropy alloy under high temperature ion irradiation, Acta Mater. 188 (2020) 1–15, https://doi.org/10.1016/j.actamat.2020.01.060.

[10] M.A. Hemphill, et al., Fatigue behavior of Al0.5CoCrCuFeNi high entropy alloys, Acta Mater. 60 (2012) 5723–5734, https://doi.org/10.1016/j.actamat.2012.06.046.

[11] S. Nellaiappan, et al., High-entropy alloys as catalysts for the Co2 and co reduction reactions: experimental realization, ACS Catal. 10 (2020) 3658–3663, https://doi.org/10.1021/acscatal.9b04302.

[12] M.H. Tsai, J.W. Yeh, High-entropy alloys: a critical review, Mater. Res. Lett. 2 (2014) 107–123, https://doi.org/10.1080/21663831.2014.912690.

[13] D.B. Miracle, O.N. Senkov, A critical review of high entropy alloys and related concepts, Acta Mater. 122 (2017) 448–511, https://doi.org/10.1016/j.actamat.2016.08.081.

[14] B. Gludovatz, A. Hohenwarter, D. Catoor, E.H. Chang, E.P. George, R.O. Ritchie, A fracture-resistant high-entropy alloy for cryogenic applications, Science 345 (6201) (1979) 1153–1158, https://doi.org/10.1126/science.1254581.

[15] F. Otto, A. Dlouhý, C. Somsen, H. Bei, G. Eggeler, and E. P. George, 'The influences of temperature and microstructure on the tensile properties of a CoCrFeMnNi high-entropy alloy', Acta Mater., vol. 61, no. 15, pp. 5743–5755, Sep. 2013, doi: https://doi.org/10.1016/j.actamat.2013.06.018.

[16] A. Gali, E.P. George, Tensile properties of high- and medium-entropy alloys, Intermetallics (Barking) 39 (2013) 74–78, https://doi.org/10.1016/j.intermet.2013.03.018.

[17] C.-J. Tong et al., 'Mechanical performance of the Al x CoCrCuFeNi high-entropy alloy system with multiprincipal elements', Metall. Mater. Trans. A, vol. 36, no. 5, pp. 1263–1271, May 2005, doi: https://doi.org/10.1007/s11661-005-0218-9.

[18] J.Y. He, et al., Effects of Al addition on structural evolution and tensile properties of the FeCoNiCrMn high-entropy alloy system, Acta Mater. 62 (1) (2014) 105–113, https://doi.org/10.1016/j.actamat.2013.09.037.

[19] Y. Liu *et al.*, 'Effect of mo element on the mechanical properties and tribological responses of cocrfenimox high-entropy alloys', Metals (Basel), vol. 11, no. 3, pp. 1–18, Mar. 2021, doi: https://doi.org/10.3390/met11030486.

[20] T. T. Shun, L. Y. Chang, and M. H. Shiu, 'Microstructure and mechanical properties of multiprincipal component CoCrFeNiMo x alloys', Mater Charact, vol. 70, pp. 63–67, Aug. 2012, doi: https://doi.org/10.1016/j.matchar.2012.05.005.

[21] W.H. Liu, et al., Ductile CoCrFeNiMox high entropy alloys strengthened by hard intermetallic phases, Acta Mater. 116 (2016) 332–342, https://doi.org/10.1016/j.actamat.2016.06.063.

[22] G. Qin, R.R. Chen, H.T. Zheng, H.Z. Fang, L. Wang, Y.Q. Su, J.J. Guo, H.Z. Fu, 'Strengthening FCC-CoCrFeMnNi high entropy alloys by Mo addition', J. Mater. Sci. Technol., vol. 35, no. 4, pp. 578–583, Apr. 2019, doi: https://doi.org/10.1016/j.jmst.2018.10.009.

[23] W.H. Liu, J.Y. He, H.L. Huang, H. Wang, Z.P. Lu, C.T. Liu, Effects of Nb additions on the microstructure and mechanical property of CoCrFeNi high-entropy alloys, Intermetallics (Barking) 60 (2015) 1–8, https://doi.org/10.1016/j.intermet.2015.01.004.

[24] T.T. Shun, L.Y. Chang, M.H. Shiu, Microstructures and mechanical properties of multiprincipal component CoCrFeNiTi x alloys, Mater. Sci. Eng. A 556 (2012) 170–174, https://doi.org/10.1016/j.msea.2012.06.075.

[25] G.A. Salishchev, et al., Effect of Mn and v on structure and mechanical properties of high-entropy alloys based on CoCrFeNi system, J. Alloys Compd. 591 (2014) 11–21, https://doi.org/10.1016/j.jallcom.2013.12.210.

[26] N.D. Stepanov, et al., Effect of v content on microstructure and mechanical properties of the CoCrFeMnNiVx high entropy alloys, J. Alloys Compd. 628 (2015) 170–185, https://doi.org/10.1016/j.jallcom.2014.12.157.

[27] J. Wang, W. Wen, J. Cheng, L. Dai, S. Li, X. Zhang, Y. Yang, H. Li, X. Hou, B. Wu, J. Wu, Tribocorrosion behavior of high-entropy alloys FeCrNiCoM (M = Al, Mo) in artificial seawater, Corros. Sci. 218 (2023), 111165, https://doi.org/10.1016/j.corsci.2023.111165.

[28] J.M. Zhu, H.F. Zhang, H.M. Fu, A.M. Wang, H. Li, Z.Q. Hu, Microstructures and compressive properties of multicomponent AlCoCrCuFeNiMox alloys, J. Alloys Compd. 497 (2010) 52–56, https://doi.org/10.1016/j.jallcom.2010.03.074.

[29] J.M. Zhu, H.M. Fu, H.F. Zhang, A.M. Wang, H. Li, Z.Q. Hu, Microstructures and compressive properties of multicomponent AlCoCrFeNiMox alloys, Mater. Sci. Eng. A 527 (2010) 6975–6979, https://doi.org/10.1016/j.msea.2010.07.028.

[30] W. Li, P. Liu, P.K. Liaw, Microstructures and properties of high-entropy alloy films and coatings: a review, Materials Research Letters 6 (4) (2018) 199–229, https://doi.org/10.1080/21663831.2018.1434248. Taylor and Francis Ltd.

[31] T. K. Chen, T. T. Shun, J. W. Yeh, and M. S. Wong, 'Nanostructured nitride films of multi-element high-entropy alloys by reactive DC sputtering', Surf Coat Technol, vol. 188–189, no. 1-3 SPEC.ISS., pp. 193–200, Nov. 2004, doi: https://doi.org/10.1016/j.surfcoat.2004.08.023.

[32] A. Xia, A. Togni, S. Hirn, G. Bolelli, L. Lusvarghi, R. Franz, Angular-dependent deposition of MoNbTaVW HEA thin films by three different physical vapor deposition methods, Surf Coat Technol 385 (2020), https://doi.org/10.1016/j.surfcoat.2020.125356.

[33] H. Zhang, Y. Pan, and Y. Z. He, 'Synthesis and characterization of FeCoNiCrCu high-entropy alloy coating by laser cladding', Mater. Des., vol. 32, no. 4, pp. 1910–1915, Apr. 2011, doi: https://doi.org/10.1016/j.matdes.2010.12.001.

[34] C. Z. Yao *et al.*, 'Electrochemical preparation and magnetic study of Bi-Fe-Co-Ni-Mn high entropy alloy', Electrochim. Acta, vol. 53, no. 28, pp. 8359–8365, Nov. 2008, doi: https://doi.org/10.1016/j.electacta.2008.06.036.

[35] V. Kouznetsov, K. Macák, J.M. Schneider, U. Helmersson, I. Petrov, A novel pulsed magnetron sputter technique utilizing very high target power densities, 1999 [Online]. Available: www.elsevier.nl/locate/surfcoat.

[36] U. Helmersson, M. Lattemann, J. Bohlmark, A.P. Ehiasarian, J.T. Gudmundsson, Ionized physical vapor deposition (IPVD): a review of technology and applications, Thin Solid Films 513 (1–2) (2006) 1–24, https://doi.org/10.1016/j.tsf.2006.03.033.

[37] K. Sarakinos, J. Alami, S. Konstantinidis, High power pulsed magnetron sputtering: a review on scientific and engineering state of the art, Surf. Coat. Technol. 204 (11) (2010) 1661–1684, https://doi.org/10.1016/j.surfcoat.2009.11.013.

[38] E. Colombini, et al., Powder metallurgy route for the synthesis of multiprincipal element alloys sputtering targets, Adv. Eng. Mater. 24 (8) (2022), https://doi.org/10.1002/adem.202101518.

[39] N.G. Kipkirui, T.T. Lin, R.S. Kiplangat, J.W. Lee, S.H. Chen, HiPIMS and RF magnetron sputtered Al0.5CoCrFeNi2Ti0.5 HEA thin-film coatings: synthesis and characterization, Surf Coat Technol 449 (2022), https://doi.org/10.1016/j.surfcoat.2022.128988.

[40] G. Greczynski, J. Lu, J. Jensen, I. Petrov, J.E. Greene, S. Bolz, W. Kölker, C. Schiffers, O. Lemmer, L. Hultman, Metal versus rare-gas ion irradiation during $Ti_{1-x}Al_xN$ film growth by hybrid high power pulsed magnetron/dc magnetron co-sputtering using synchronized pulsed substrate bias, J. Vac. Sci. Technol. A 30 (6) (2012), 061504, https://doi.org/10.1116/1.4750485.

[41] G. Greczynski, I. Zhirkov, I. Petrov, J.E. Greene, J. Rosen, Control of the metal/gas ion ratio incident at the substrate plane during high-power impulse magnetron sputtering of transition metals in Ar, Thin Solid Films 642 (2017) 36–40, https://doi.org/10.1016/j.tsf.2017.09.027.

[42] Jian-Fu Tang, Shi-Yu Huang, Ja-Hon Lin, Fu-Chi Yang, Chi-Lung Chang, Mechanical properties of TiN deposited in synchronous bias mode through high-power impulse magnetron sputtering, Surf. Coat. Technol. 434 (2022), 128201, https://doi.org/10.1016/j.surfcoat.2022.128201.

[43] G.G. Stoney, 'The tension of metallic films deposited by electrolysis', Proceedings of the Royal Society of London. Series A, Containing Papers of a Mathematical and Physical Character 82 (553) (1909) 172–175, https://doi.org/10.1098/rspa.1909.0021.

[44] W.D. Nix, Mechanical properties of thin films, Metall. Trans. A. 20 (11) (1989) 2217–2245, https://doi.org/10.1007/BF02666659.

[45] A.M. Korsunsky, M.R. McGurk, S.J. Bull, T.F. Page, On the hardness of coated systems, Surf Coat Technol 99 (1–2) (1998) 171–183, https://doi.org/10.1016/S0257-8972(97)00522-7.

[46] W.C. Oliver, G.M. Pharr, An improved technique for determining hardness and elastic modulus using load and displacement sensing indentation experiments, J. Mater. Res. 7 (6) (1992) 1564–1583, https://doi.org/10.1557/jmr.1992.1564.

[47] W.C. Oliver, G.M. Pharr, Measurement of hardness and elastic modulus by instrumented indentation: advances in understanding and refinements to methodology, J Mater Res 19 (1) (2004) 3–20, https://doi.org/10.1557/jmr.2004.19.1.3.

[48] J.J. Wang, F.Y. Ouyang, Nanotwinned medium entropy alloy CoCrFeNi thin films with ultra-high hardness: modifying residual stress without scarifying hardness through tuning substrate bias, Surf Coat Technol 434 (2022), https://doi.org/10.1016/j.surfcoat.2022.128191.

[49] N. Laegreid, G.K. Wehner, Sputtering yields of metals for Ar^+ and ne^+ ions with energies from 50 to 600 ev, J. Appl. Phys. 32 (3) (1961) 365–369, https://doi.org/10.1063/1.1736012.

[50] S. Guo, C. Ng, J. Lu, C.T. Liu, Effect of valence electron concentration on stability of fcc or bcc phase in high entropy alloys, J. Appl. Phys. (2011), https://doi.org/10.1063/1.3587228.

[51] C.J. Tong, Y.L. Chen, S.K. Chen, J.W. Yeh, T.T. Shun, C.H. Tsau, S.J. Lin, S. Y. Chang, Mechanical performance of the Al x CoCrCuFeNi high-entropy alloy system with multiprincipal elements, Metall. Mater. Trans. 36A (2005) 881, https://doi.org/10.1007/s11661-005-0218-9.

[52] Y. Zhao, X. Zhang, H. Quan, Y. Chen, S. Wang, S. Zhang, Effect of Mo addition on structures and properties of FeCoNiCrMn high entropy alloy film by direct current magnetron sputtering, J. Alloys Compd. 895 (2022), https://doi.org/10.1016/j.jallcom.2021.162709.

[53] G. O. Boakye *et al.*, 'Microstructural properties and Wear resistance of Fe-Cr-Co-Ni-Mo-based high entropy alloy coatings deposited with different coating techniques', Applied Sciences (Switzerland), vol. 12, no. 6, Mar. 2022, doi: https://doi.org/10.3390/app12063156.

[54] F. Otto, Y. Yang, H. Bei, E.P. George, Relative effects of enthalpy and entropy on the phase stability of equiatomic high-entropy alloys, Acta Mater. 61 (7) (2013) 2628–2638, https://doi.org/10.1016/j.actamat.2013.01.042.

[55] T.H. Fang, W.L. Li, N.R. Tao, K. Lu, Revealing extraordinary intrinsic tensile plasticity in gradient nano-grained copper, Science (1979) 331 (6024) (2011) 1587–1590, https://doi.org/10.1126/science.1200177.
[56] K. Lu, L. Lu, S. Suresh, Strengthening materials by engineering coherent internal boundaries at the nanoscale, Science (1979) 324 (5925) (2009) 349–352, https://doi.org/10.1126/science.1159610.
[57] A.L. Patterson, The Scherrer Formula for I-Ray Particle Size Determination, 1939.
[58] X. Sauvage, P. Jessner, F. Vurpillot, R. Pippan, Nanostructure and properties of a cu-Cr composite processed by severe plastic deformation, Scr. Mater. 58 (12) (2008) 1125–1128, https://doi.org/10.1016/j.scriptamat.2008.02.010.
[59] T.T. Shun, L.Y. Chang, M.H. Shiu, Age-hardening of the CoCrFeNiMo0.85 high-entropy alloy, Mater Charact 81 (2013) 92–96, https://doi.org/10.1016/j.matchar.2013.04.012.
[60] A.J. Zaddach, C. Niu, C.C. Koch, D.L. Irving, Mechanical properties and stacking fault energies of NiFeCrCoMn high-entropy alloy, JOM 65 (12) (2013) 1780–1789, https://doi.org/10.1007/s11837-013-0771-4.
[61] J.A. Thornton, D.W. Hoffman, Stress-related effects in thin films, Thin Solid Films 171 (1) (1989) 5–31, https://doi.org/10.1016/0040-6090(89)90030-8.
[62] S. Fang, et al., Microstructures and mechanical properties of CoCrFeMnNiVx high entropy alloy films, J. Alloys Compd. 820 (2020), https://doi.org/10.1016/j.jallcom.2019.153388.
[63] C. Sha, Z. Zhou, Z. Xie, P. Munroe, High entropy alloy FeMnNiCoCr coatings: enhanced hardness and damage-tolerance through a dual-phase structure and nanotwins, Surf Coat Technol 385 (2020), https://doi.org/10.1016/j.surfcoat.2020.125435.
[64] T.H. Huang, C.H. Hsueh, Microstructures and mechanical properties of (CoCrFeMnNi)100-xMox high entropy alloy films, Intermetallics (Barking) 135 (2021), https://doi.org/10.1016/j.intermet.2021.107236.
[65] B. Braeckman, F. Misják, G. Radnóczi, M. Caplovicová, P. Djemia, F. Tétard, L. Belliard, D. Depla, The nanostructure and mechanical properties of nanocomposite Nbx-CoCrCuFeNi thin films, Scr. Mater. 139 (2017) 155–158, https://doi.org/10.1016/j.scriptamat.2017.06.046.
[66] R.W. Cahn, P. Hassen, Physical Metallurgy 4th ed., vol. 1, 1996 (North Holland, Amsterdam.
[67] Y. Zhang, Y.J. Zhou, J.P. Lin, G.L. Chen, P.K. Liaw, Solid-solution phase formation rules for multi-component alloys, Adv. Eng. Mater. 10 (6) (2008) 534–538, https://doi.org/10.1002/adem.200700240.
[68] X. Yang, Y. Zhang, Prediction of high-entropy stabilized solid-solution in multi-component alloys, Mater. Chem. Phys. 132 (2–3) (2012) 233–238, https://doi.org/10.1016/j.matchemphys.2011.11.021.
[69] X. Yang, S.Y. Chen, J.D. Cotton, Y. Zhang, Phase stability of low-density, multiprincipal component alloys containing aluminum, magnesium, and lithium, JOM J. Miner. Met. Mater. Soc. 66 (2014) 2009–2020, https://doi.org/10.1007/s11837-014-1059-z.
[70] S. Fang, X. Xiao, L. Xia, W. Li, Y. Dong, Relationship between the widths of supercooled liquid regions and bond parameters of Mg-based bulk metallic glasses, J. Non Cryst. Solids 321 (1–2) (2003) 120–125, https://doi.org/10.1016/S0022-3093(03)00155-8.
[71] A. Takeuchi, A. Inoue, Classification of bulk metallic glasses by atomic size difference, heat of mixing and period of constituent elements and its application to characterization of the Main alloying element, Mater. Trans. 46 (12) (2005) 2817–2829, https://doi.org/10.2320/matertrans.46.2817.
[72] S. Guo, C.T. Liu, Phase stability in high entropy alloys: formation of solid-solution phase or amorphous phase, Prog. Nat. Sci.: Mater. Int. 21 (6) (2011) 433–446, https://doi.org/10.1016/S1002-0071(12)60080-X.
[73] Z. Tang, et al., Aluminum alloying effects on lattice types, microstructures, and mechanical behavior of high-entropy alloys systems, JOM 65 (12) (2013) 1848–1858, https://doi.org/10.1007/s11837-013-0776-z.
[74] F. Cao, P. Munroe, Z. Zhou, Z. Xie, Medium entropy alloy CoCrNi coatings: enhancing hardness and damage-tolerance through a nanotwinned structuring, Surf Coat Technol 335 (2018) 257–264, https://doi.org/10.1016/j.surfcoat.2017.12.021.
[75] P. Nagy, et al., Processing and characterization of a multibeam sputtered nanocrystalline CoCrFeNi high-entropy alloy film, Surf. Coat. Technol. 386 (2020), https://doi.org/10.1016/j.surfcoat.2020.125465.
[76] Y. Dong, Y. Lu, J. Kong, J. Zhang, T. Li, Microstructure and mechanical properties of multi-component AlCrFeNiMo x high-entropy alloys, J. Alloys Compd. 573 (2013) 96–101, https://doi.org/10.1016/j.jallcom.2013.03.253.
[77] E.O. Hall, The deformation and ageing of mild steel: III discussion of results, Proceedings of the Physical Society. Section B 64 (9) (1951) 747–753, https://doi.org/10.1088/0370-1301/64/9/303.
[78] N.J. Petch, The cleavage strength of polycrystals, Journal of the Iron and Steel Institute 174 (1953) 25–28.
[79] X. Zhang, et al., Enhanced hardening in Cu/330 stainless steel multilayers by nanoscale twinning, Acta Mater. 52 (4) (2004) 995–1002, https://doi.org/10.1016/j.actamat.2003.10.033.
[80] X. Zhang, et al., Nanoscale-twirming-induced strengthening in austenitic stainless steel thin films, Appl. Phys. Lett. 84 (7) (2004) 1096–1098, https://doi.org/10.1063/1.1647690.
[81] L. Lu, Y. Shen, X. Chen, L. Qian, K. Lu, Ultrahigh strength and high electrical conductivity in copper, Science (1979) 304 (5669) (2004) 422–426, https://doi.org/10.1126/science.1092905.
[82] Y.F. Shen, L. Lu, Q.H. Lu, Z.H. Jin, K. Lu, Tensile properties of copper with nano-scale twins, Scr. Mater. 52 (10) (2005) 989–994, https://doi.org/10.1016/j.scriptamat.2005.01.033.
[83] N. Chawake, et al., Microstructural characterization of medium entropy alloy thin films, Scr. Mater. 177 (Mar. 2020) 22–26, https://doi.org/10.1016/j.scriptamat.2019.10.001.
[84] J. Miao, T. Guo, J. Ren, A. Zhang, B. Su, J. Meng, Optimization of mechanical and tribological properties of FCC CrCoNi multi-principal element alloy with Mo addition, Vacuum 149 (Mar. 2018) 324–330, https://doi.org/10.1016/j.vacuum.2018.01.012.